***PREPRINT**: Blocken B, Carmeliet J. 2006. The influence of the wind-blocking effect by a building on its wind-driven rain exposure. Journal of Wind Engineering and Industrial Aerodynamics 94(2): 101-127. © Elsevier 2006.*

The influence of the wind-blocking effect by a building on its wind-driven rain exposure

Bert Blocken* [(a)], Jan Carmeliet [(a,b)]

(a) Laboratory of Building Physics, Department of Civil Engineering, Katholieke Universiteit Leuven, Kasteelpark Arenberg 40, 3001 Leuven, Belgium
(b) Building Physics Group, Faculty of Building and Architecture, Technical University Eindhoven, P.O. box 513, 5600 MB Eindhoven, The Netherlands

Abstract

Wind-driven rain (WDR) is one of the most important moisture sources that affect the hygrothermal performance and the durability of building facades. The complexity of WDR has led to the use of Computational Fluid Dynamics (CFD) to predict the amount of WDR falling onto building facades. Recently, the CFD model for WDR simulation has been successfully validated for a low-rise building of complex geometry and for a range of rain events, providing confidence for further numerical studies. In this paper, the influence of the wind-blocking effect by a building on its WDR exposure is examined. Part of the latest WDR CFD validation study for the VLIET building and CFD simulations of the WDR distribution on four different single-building configurations are presented. It is shown that the wind-blocking effect is one of the main factors that govern the WDR distribution pattern. As a result, high-rise buildings do not necessarily catch more WDR than low-rise buildings.

Keywords: Wind-driven rain; Driving rain; Wind flow; Raindrop trajectories; Impact; Wetting pattern; Catch ratio; Building; Computational Fluid Dynamics (CFD); Validation

1. Introduction

Wind-driven rain (WDR) is an essential boundary condition in many research areas (building physics, earth sciences, hydrology, meteorology, etc.). In building physics, WDR is one of the most important moisture sources affecting building facades. Information concerning the exposure to WDR is essential to design building facades with a satisfactory hygrothermal performance. Knowledge on the quantity of WDR is also an essential requirement as a boundary condition for Heat-Air-Moisture (HAM) transfer analysis. In the past, a number of methods have been developed and employed to quantify WDR: experimental, semi-empirical and numerical methods. A review on the assessment of WDR in building research can be found in [1].

As experimental and semi-empirical research efforts continued to reveal the inherent complexity of WDR, researchers realized that further achievements were to be made through numerical analyses. Souster (1979, [2]) was the first to study raindrop trajectories based on computed flow patterns around 2D buildings, introducing Computational Fluid Dynamics (CFD) in WDR research. CFD comprises the use of numerical techniques to obtain the wind-flow pattern. The bulk of numerical WDR research has been conducted in the past 15 years. The work of Choi [3-5] has been the break-through for the use of numerical methods in WDR research. He presented a numerical simulation technique where the raindrop trajectories are calculated based on a steady-state 3D CFD wind-flow pattern. This technique allows determining the spatial distribution of WDR on buildings under steady-state conditions of wind and rain, i.e. for a fixed, static value of wind speed, wind direction and horizontal rainfall intensity (i.e. the rainfall intensity falling through a horizontal plane). These publications and following contributions considerably extended the existing knowledge (e.g. [6-9]). In 2000, Blocken and Carmeliet [10] extended Choi's simulation technique by adding the temporal component and by developing a new weighted data-averaging technique, allowing the numerical determination of both the spatial and temporal distribution of WDR on buildings. Recent validation studies for a low-rise building and for different rain events have indicated that this extended numerical method can provide quite accurate predictions of the WDR amount and the WDR distribution on a building facade [10]. These validation studies have provided confidence for further numerical studies.

* Corresponding author: Bert Blocken, Laboratory of Building Physics, K.U.Leuven, Kasteelpark Arenberg 40, 3001 Leuven, Belgium. Tel.: +32 (0) 16-321345 - Fax: +32 (0) 16-321980
E-mail address: bert.blocken@bwk.kuleuven.be

This paper presents a numerical investigation of the influence of the wind-blocking effect by a single-standing building on its WDR exposure. The wind-blocking effect refers to the disturbance of the wind-flow pattern by the presence of the building. In this paper, the focus is on the decrease of the streamwise horizontal wind-velocity component upstream of the building (wind-speed slow-down). As part of this study, CFD simulations of WDR on the windward facades of four different building configurations were conducted and compared: (1) a low-rise cubic building; (2) a medium-rise wide slab; (3) a high-rise slab; and (4) a tower building. First, in section 2, the specific catch ratio and the catch ratio are defined and the influencing parameters are given. In section 3, the numerical WDR model that is used to calculate the catch ratio and the WDR amount is briefly outlined. Section 4 briefly presents part of a recent, more detailed validation effort than [10]. It supports the simulations in this study and it was also the direct cause for investigating the influence of the wind-blocking effect. In sections 5 and 6, the simulation results for the four different building configurations are presented and compared and the influence of the wind-blocking effect is discussed. Finally, sections 7 and 8 provide a general discussion and the conclusions.

2. Definitions and parameters

The quantities that are used to describe the WDR intensity are the specific catch ratio $\eta_d(d)$, related to the raindrop diameter d, and the catch ratio η, related to the entire spectrum of raindrop diameters (Eq. 1):

$$\eta_d(d) = \frac{R_{wdr}(d)}{R_h(d)} \quad ; \quad \eta = \frac{R_{wdr}}{R_h} \tag{1}$$

where $R_{wdr}(d)$ and $R_h(d)$ are the specific WDR intensity on the building and the specific unobstructed horizontal rainfall intensity, respectively. R_{wdr} and R_h respectively refer to the same quantities but integrated over all raindrop diameters. The unobstructed horizontal rainfall intensity is the intensity of rainfall through a horizontal plane that is situated outside the wind-flow pattern that is disturbed by the building (i.e. the rainfall that would be measured by a rain gauge with a horizontal orifice at ground-level, placed in an open field).

The catch ratio η is a complex function of space and time. The six basic influencing parameters for η are: (1) the building geometry (including environment topology), (2) the position on the building facade, (3) the reference wind speed, (4) the reference wind direction, (5) the horizontal rainfall intensity and (6) the horizontal raindrop-size distribution. In reality, the turbulent dispersion of raindrops is an additional parameter. It is often neglected, as will be done in this paper. This decision is based on the findings by Choi [11] and by Blocken and Carmeliet [10] and on a review of the literature [1]. The reference wind speed U_{10} (m/s) refers to the horizontal component of the wind-velocity vector at 10 m height in the upstream undisturbed flow. The reference wind direction φ_{10} (degrees from north) refers to the direction of the reference wind speed. The horizontal raindrop-size distribution $f_h(d)$ (m^{-1}) refers to the raindrop-size distribution as a flux through a horizontal plane.

3. Numerical wind-driven rain model

The numerical model for the simulation of WDR on buildings, developed by Choi [3-5] and extended by Blocken and Carmeliet [10], consists of five steps:

1. The steady-state wind-flow pattern around the building is calculated using a CFD code.
2. Raindrop trajectories are obtained by injecting raindrops of different sizes in the calculated wind-flow pattern and by solving their equations of motion.
3. The specific catch ratio is determined based on the configuration of the calculated raindrop trajectories.
4. The catch ratio is calculated from the specific catch ratio and from the raindrop-size distribution.
5. From the data in the previous step, catch-ratio charts are constructed for different zones (positions) at the building facade. The experimental data record of reference wind speed, wind direction and horizontal rainfall intensity for a given rain event is combined with the appropriate catch-ratio charts to determine the corresponding spatial and temporal distribution of WDR on the building facade.

The five steps are described in more detail below. The steady-state wind-flow pattern is usually obtained by solving the Reynolds-Averaged Navier-Stokes (RANS) equations in combination with a k-ε turbulence model. The equation of motion of a raindrop, moving in a wind-flow field characterized by a mean velocity vector $\vec{V}$ is:

$$\left(\frac{\rho_w - \rho}{\rho_w}\right)\vec{g} + \frac{3\mu}{\rho_w d^2}\cdot\frac{C_d Re_R}{4}\cdot\left(\vec{V} - \frac{d\vec{r}}{dt}\right) = \frac{d^2\vec{r}}{dt^2} \tag{2}$$

where Re_R is the relative Reynolds number (referring to the airflow around the raindrop):

$$Re_R = \frac{\rho d}{\mu} \left\| \vec{V} - \frac{d\vec{r}}{dt} \right\| \quad (3)$$

and ρ_w is the density of the raindrop, ρ the density of the air, g the gravitational acceleration, μ the dynamic air viscosity, d the raindrop diameter, C_d the raindrop drag coefficient, $\vec{r}$ the position vector of the raindrop in the xyz-space and t the time co-ordinate. The calculation of the specific catch ratio (η_d) and the catch ratio (η) is performed for a number of zones on the building facade (e.g. zone A_f in Fig. 1). For each zone, the same procedure is employed. In the steady-state wind-flow pattern – thus neglecting the turbulent dispersion of raindrops – raindrop trajectories of diameter d ending on the corner points of the zone form a stream tube (Fig. 1). Conservation of mass for the raindrops in the stream tube allows η_d to be expressed in terms of areas:

$$\eta_d(d) = \frac{R_{wdr}(d)}{R_h(d)} = \frac{A_h(d)}{A_f} \quad (4)$$

where A_f is the area of the zone on the building facade where η_d is to be determined and $A_h(d)$ is the area of the horizontal plane bounded by the injection positions of the raindrops of diameter d ending on the corner points of A_f. This plane $A_h(d)$ is located in the upstream undisturbed wind flow. Its location must allow the raindrops injected at that position to reach their terminal velocity of fall (vertical) and the wind velocity (horizontal) before entering the flow pattern that is disturbed by the presence of the building. The catch ratio η for a zone is obtained by multiplying η_d for each raindrop diameter d for this zone with the fraction of these drops in the spell (horizontal raindrop-size distribution $f_h(d)$) and integrating over all raindrop diameters:

$$\eta = \int_d f_h(d)\,\eta_d(d)\,dd \quad (5)$$

It is important to note that for describing raindrop-size distributions, a probability-density function f(d) is usually provided that refers to the distribution of raindrops in a volume of air. For use in the present model however (where we deal with fluxes) the raindrop-size distribution f(d) applying to a volume of air has to be converted to the raindrop-size distribution as a flux through a horizontal plane $f_h(d)$; i.e. the horizontal raindrop-size distribution. The reason is that, due to the variation of the terminal velocity of fall V_t of a raindrop with size, the raindrop-size distribution in the air differs from the raindrop-size distribution through a horizontal plane. The former can be converted to the latter by multiplying with the raindrop terminal velocity of fall (Eq. 6). The denominator in this equation is necessary to ensure that the area under the curve of the probability-density function $f_h(d)$ is equal to unity.

$$f_h(d) = \frac{f(d)\,V_t(d)}{\int_d f(d)\,V_t(d)\,dd} \quad (6)$$

In this model, the raindrop-size distribution of Best [12] is adopted. This size distribution is characterized by a unique relationship between the horizontal rainfall intensity R_h and the (horizontal) raindrop-size distribution $f_h(d)$. Let us recall the six basic influencing parameters of the catch ratio mentioned in section 2. For a given building geometry, for a given position on the building facade, for a given wind direction and adopting the raindrop-size distribution according to Best [12], the catch ratio is unambiguously defined by two parameters: the reference wind speed U_{10} and the horizontal rainfall intensity R_h. Therefore, the catch ratio η for a given zone (position) on the building facade is typically presented in a catch-ratio chart with η as a function of U_{10} and R_h for a given wind direction φ_{10} [10] (e.g. Fig. 2). To determine the WDR amount on the building facade, the catch-ratio charts are combined with meteorological data records of U_{10}, φ_{10} and R_h (rain events). The data records are partitioned into a number of equidistant time steps (e.g. 10-minute intervals). Each time step is considered steady-state and the meteorological data for each time step are used to extract the corresponding catch ratio from the appropriate catch-ratio chart. Multiplying each catch-ratio value with the corresponding horizontal rainfall amount S_h for that time step yields the WDR amount for that time step: S_{wdr}.

4. Model validation

Part of a recent, quite detailed validation study is presented. This study supports the additional numerical simulations reported in this paper and it was also the direct cause for investigating the influence of the wind-blocking effect.

4.1. Full-scale measurements

The validation study was based on a high-resolution experimental WDR database for the low-rise VLIET test building of the Laboratory of Building Physics, Katholieke Universiteit Leuven. The design and installation of the measurement set-up and the experimental data have been described in detail in an earlier publication [13]. Only the headlines will be repeated here. The building consists of two main modules, the flat-roof module and the sloped-roof module (Fig. 3). In between the main modules, there is a small terrace module. The building is 25.2 m long and 7.2 m wide. The height of the flat-roof module and the sloped-roof module is 4.3 m and 7.9 m respectively. The terrace height is 3.95 m. Roof overhang varies along the length axis of the building as indicated in Fig. 3. The database focused on south-west wind direction. A view of the terrain situated south-west of the test building is provided in Fig. 4. The elements providing shielding from wind in the direct vicinity of the building are some low agricultural constructions to the south and a row of high trees (poplars) to the west side. It is situated closest to the sloped-roof-module corner. The measurement set-up consists of (1) a meteorological mast positioned in front of the south-west facade that is equipped with three cup anemometers and one ultrasonic anemometer (Fig. 5); (2) a capacitance rain gauge placed behind a semi-circular turf wall (Fig. 5); and (3) a large number of WDR gauges (0.2x0.2m² catch area) mainly spread across the south-west facade (Fig. 3). The wind-speed profile measured by the meteorological mast for south-west wind corresponds to a power law with exponent $\alpha = 0.176$ [13]. The data were gathered on a 1-minute basis. For the validation study to be reliable, high quality of the experimental data is required, imposing demands on accuracy and reliability. This has been ensured by strictly following the guidelines for WDR gauge design, WDR measurement error estimation and WDR data selection that were provided in [13,14].

4.2. Simulation characteristics and settings

The wind-flow pattern around the VLIET test building was modelled with the commercial CFD code Fluent 5.4 using the RANS approach. The characteristics of the CFD simulation are listed in Table 1. The following important aspects are mentioned explicitly. (1) The building model stands alone on a large plain covered with short grass (corresponding to aerodynamic roughness length $y_0 = 0.03$ m [15]). The row of trees was not included in the model. It is expected that the trees will somewhat slow down the approach-flow wind speed and this effect will be more pronounced for the west corner of the building (sloped-roof module) than for the south corner (flat-roof module). (2) The upstream length of the computational domain is deliberately taken longer than would be needed for wind-flow calculations only. It is determined by the location of the upstream injection positions of the raindrops that will end on the building facade. (3) A suitable numerical grid was obtained based on grid-sensitivity analysis. (4) The inlet wind speed profile was taken from the measurements. (5) The simulations were conducted for south-west wind (225° from north), i.e. perpendicular to the south-west facade. (6) Standard wall functions [17] modified for roughness based on the formulae by Cebeci and Bradshaw [18] were used. To avoid the use of excessively large cells near the ground for these wall functions [19,20], the physical ground roughness K_S in the CFD code was taken equal to the aerodynamic roughness length $y_0 = 0.03$ m and in order to achieve horizontal homogeneity of the approach-flow mean wind-speed profile, the inlet turbulent kinetic energy k had to be reduced from $3.33(u^*_{ABL})^2$ to $1.5(u^*_{ABL})^2$, where u^*_{ABL} is the friction velocity associated with the simulation inlet profiles. For more information on this matter, the reader is referred to [19,20]. (7) Turbulent dispersion of the raindrops is neglected.

The calculation of the raindrop trajectories, the specific catch ratio and the catch ratio were performed with author-written program codes. The characteristics and settings for the integration procedure to solve Eq. (2) and for the integration procedure for Eq. (5) and (6) are given in Table 2.

4.3. Simulation results and validation

The numerical simulation of the wind-flow pattern was performed for a reference wind speed $U_{10} = 10$ m/s. The wind-velocity vector fields for other reference wind-speed values were obtained by linear scaling with U_{10}, which is allowed for flows around sharp-edged bluff bodies, where the positions of flow separation are independent of the Reynolds number. Calculations of the raindrop motions were conducted in flow patterns with U_{10} = 1, 2, 3, 4, 5, 6, 8 and 10 m/s. The catch ratio η at each position on the windward facade was determined for each reference wind speed and for the following horizontal rainfall intensities: R_h = 0, 0.1, 0.5, 1, 2, 3, 4, 5, 6, 8,

10, 12, 15, 20, 25, 30 mm/h. From this information, catch-ratio charts were constructed. Based on these charts, the spatial and temporal distribution of WDR on the VLIET building for a range of different rain events was determined.

Only the results for one rain event (Fig. 6) are presented here. The wind speed in this rain event is quite low, ranging between 0.5 and 5 m/s. The wind direction during rain is approximately south-west (225°). The rain event is mainly composed of three rain showers, one with heavy (8 mm/h), one with moderate (4 mm/h) and one with light (2 mm/h) rainfall intensity, respectively. The total horizontal rainfall amount S_h = 11.3 mm. The spatial distribution of the ratio S_{wdr}/S_h at the end of the rain event (accumulated WDR amount at each facade position divided by accumulated horizontal rainfall amount) is given in Fig. 7. Fig. 7a-b illustrate the numerical results. The areas of the facade that are sheltered from rain by the roof overhang are coloured black (S_{wdr} = 0) (Fig. 7b). High WDR exposure is observed at the top of the terrace module, where there is no roof overhang. The values indicated in the rectangular boxes (Fig. 7b) are the calculation results at the positions of the WDR gauges. They can be directly compared to the corresponding measurement results in Fig. 7c. The estimated measurement error for the ratio S_{wdr}/S_h is e_{wdr} = 0.05 [13,14]. Generally, the agreement between numerical and experimental results is good. The distinct wetting pattern found in the simulations is corroborated by the measurements. Some overestimations by the numerical method are noted. Large discrepancies (overestimations) however are present at the sloped-roof-module corner (positions 2-3). This can – at least partly – be explained by the retarding effect by the row of trees on the wind flow (which is not included in the model but which is present in reality).

An important observation in Fig. 7 is that the flat-roof-module facade receives significantly more WDR than the sloped-roof-module facade. This has been observed systematically for all measurements and all simulations that were conducted. It can be partly attributed to the larger roof overhang length for the sloped-roof module. But one could argue that it is also in part caused by the wind-blocking effect. The simulation results of the wind-flow pattern indicated lower streamwise wind-speed values in front of the sloped-roof module than in front of the flat-roof module. This could mean that the higher sloped-roof module presents a larger obstruction to the upstream wind-flow field. As a result, it would provide a more important streamwise wind-speed slow-down and therefore this module would receive less WDR. The confirmation of this hypothesis is complicated by the rather complex geometry of the VLIET building, especially the presence of variable roof overhang lengths. Therefore, an investigation based on CFD simulations for simple, generic building configurations was conducted.

5. Model application for different building configurations

5.1. Simulation characteristics and settings

The numerical simulations were conducted for four different single-building models that are representative for a certain range of real buildings. The dimensions of these rectangular models are given in Table 3. The simulation characteristics and settings were as much as possible identical to those for the validation study in the previous section. The most important differences are the size of the computational domain and the number of control volumes: (1) for the low-rise cubic building: domain size LxBxH = 310x110x60 m³, 1063881 control volumes; (2) for the medium-rise building: domain size LxBxH = 1210x700x200 m³, 950469 control volumes; (3) for the high-rise building slab: domain size LxBxH = 1210x550x300 m³, 813002 control volumes; (4) for the tower building: domain size LxBxH = 1210x550x300 m³, 694860 control volumes. The following important aspects are mentioned explicitly. (1) The building models stand alone on a large plain covered with short grass (y_0 = 0.03 m). (2) The four numerical grids were obtained based on grid-sensitivity analyses. (3) The wind-flow calculations were performed with a power-law inlet wind-speed profile with exponent α_P = 0.15, corresponding to y_0 = 0.03 m. (4) The wind direction is perpendicular to the windward facade. (5) For horizontal homogeneity of the mean wind-speed profile the inlet turbulent kinetic was reduced from $3.33(u^*_{ABL})^2$ to $0.75(u^*_{ABL})^2$.

5.2. Simulation results

The numerical simulations were performed for the same wind-speed values, raindrop diameters and horizontal rainfall intensities as mentioned in Table 2 and subsection 4.3. For these simulations, only the first four steps in the WDR model (section 3) were executed. The results are provided in the following ways:

1. Contours of the streamwise horizontal wind-velocity component U in a vertical plane through the center of the building. The values are made dimensionless by division by the reference wind speed U_{10}. The contours are only displayed upstream of the building, because the focus is on WDR hitting the windward facade. They serve to illustrate to what extent the building slows down the wind speed in front of it (wind-blocking effect).
2. Trajectories of 1 mm diameter drops in the U_{10} = 10 m/s wind-flow field, upstream of the windward facade, in the same vertical plane.
3. Contours of the catch ratio on the windward facade, for U_{10} = 10 m/s and R_h = 1, 10 and 30 mm/h.

4. Catch-ratio charts for two positions on each facade, illustrating η as a function of U_{10} and R_h.

For each building, the simulation results are briefly described below.

5.2.1. Low-rise cubic building

Fig. 8a presents the building configuration, the building dimensions, the approach-flow profile and positions 1 and 2 at the windward facade. Figs. 8b-h present the numerical simulation results. Fig. 8b shows the contours of U/U_{10} in a vertical plane through the center of the building. It is clear that the wind-blocking effect is not very pronounced upstream of the building: only a minor disturbance of the wind-flow field is observed. Fig. 8c displays trajectories of 1 mm diameter raindrops in the U_{10} = 10 m/s wind-flow field. Due to the small wind-blocking effect, the trajectories ending upstream of the windward facade are almost rectilinear and only show a small curvature at their ends. Figs. 8d-f illustrate the spatial variation of the catch ratio across the windward facade, for U_{10} = 10 m/s and R_h = 1, 10, 30 mm/h. The typical features of WDR wetting patterns on building facades are observed: (1) The η-values increase from bottom to top and from the middle of the facade to the sides; (2) The highest values are found at the top edge and at the top corners of the facade; (3) The wetting gradient is highest near the top edge (in the vertical direction) and near the top corners. In earlier studies [4,5,9,10], it was shown that smaller raindrops are more influenced by the local wind-flow pattern than larger drops, and that therefore the wetting gradients from bottom to top of facades are most pronounced for the lower rainfall intensities that contain a larger fraction of small drops. This is also indicated by this study: as R_h increases, the maximum catch ratio on the facade decreases and the minimum catch ratio increases. Note however that the general wetting pattern is very similar for all three R_h-values. Figs. 8g-h display the catch-ratio charts for position 1 and 2 at the top edge of the facade. The observations are: (1) At positions 1 and 2, η shows a steep increase for light R_h and levels out as R_h increases; (2) At positions 1 and 2, η varies approximately linearly with U_{10}. It must be noted that at other positions on the facade, the η-charts have somewhat different shapes and that at these positions, the dependency on R_h can be more pronounced (e.g. Fig. 2 and [10]).

5.2.2. Medium-rise, wide building slab

Fig. 9b indicates that the wind-blocking effect is clearly present for a considerable distance upstream of the building. This is indicated by the elevation of the isoline $U/U_{10} = 1$ above its free-field location at a height $y = 10$ *m* above ground (dashed line in Fig. 9b). The corresponding decrease in streamwise horizontal wind speed causes a decrease of the streamwise horizontal raindrop speed. As a result, the raindrop trajectories ending close to the windward building facade show a downward curvature (Fig. 9c). Figs. 9d-f illustrate the η-contours for U_{10} = 10 m/s and R_h = 1, 10, 30 mm/h. Due to the downward curvature of the trajectories, wetting is less pronounced at the lower part of the facade, for low as well as for high R_h. Figs. 9g-h are the η-charts at position 1 and 2. Concerning these charts, similar observations as for the low-rise cubic building can be made.

5.2.3. High-rise building slab

Fig. 10b shows that the wind-blocking effect is very pronounced: a significant decrease of the streamwise horizontal wind-velocity component is found for a considerable distance upstream of the building. This decrease of the driving force for WDR causes the trajectories of the raindrops that traverse this region to become more vertical (Fig. 10c). As a result, only a relatively small amount of WDR will hit the lower parts of the facade. Figs. 10d-f show the η-contours: a remarkable feature of the wetting pattern is that the lower part of the facade remains relatively dry. This is most pronounced at lower R_h-values, because the trajectories of smaller raindrops are more influenced by the wind-blocking effect. The wetting gradients are only pronounced at the upper part of the facade. Figs. 10g-h illustrate the catch-ratio charts.

5.2.4. Tower building

Fig. 11b shows that the wind-blocking effect is quite significant. The raindrop trajectories (Fig. 11c) ending on the lowest three quarters of the building show a downward curvature, indicating that they have traversed a region that is more subjected to the wind-blocking effect. Figs. 11d-f show that wetting is indeed not very pronounced at the lower portions of the facade. Wetting and the wetting gradients are pronounced at the upper part. As R_h increases, wetting at the lower part increases, but the general wetting pattern remains quite similar for the different R_h-values. Figs. 11g-h are the catch ratio charts at position 1 and 2.

6. Comparison of the results

First, Figs. 8b, 9b, 10b, 11b containing the wind-flow patterns are compared, as well as Figs. 8c, 9c, 10c, 11c displaying the raindrop trajectories. For comparison purposes, the scale in all these figures is the same, and in all figures, the raindrop trajectories were injected equidistantly at 25 m intervals from a straight horizontal line. In Figs. 8b, 9b, 10b and 11b, the presence and the extent of the wind-blocking effect is indicated by the elevation of the isoline $U/U_{10} = 1$ above its free-field location at a height $y = 10$ *m* above ground (see dashed lines in the figures). The wind-blocking effect is most pronounced for the high-rise building slab, and least pronounced for the low-rise cubic building. It is stronger for the high-rise slab than for the tower building, due to the limited width of the tower. The influence of the wind-blocking effect is indicated by comparing Figs. 8c, 9c, 10c and 11c. The larger the region where the wind-blocking effect acts and the stronger this effect, the more the streamwise horizontal raindrop speed will decrease, yielding – among others – raindrop trajectories that are almost vertical close to the lower part of the windward building facade. Note that only trajectories for 1 mm diameter drops are shown in these figures. For smaller drops, this effect will be somewhat more pronounced, while for larger drops, it will be somewhat less pronounced. The implications of the wind-blocking effect on the catch-ratio values and the wetting patterns are discussed in more detail in the following paragraphs.

A comparison is made between the maximum η-values (building top corners; see Figs. 8d-f, 9d-f, 10d-f and 11d-f) for different R_h, ranging from very light (0.1 mm/h) to extremely heavy (100 mm/h): Table 4. The η-values are quite different for the different buildings. The differences are largest for low R_h and decrease as R_h increases. Note that from all buildings, the high-rise slab top corner is always least exposed to WDR and that up to at least R_h = 10 mm/h, the cubic building top corner is most exposed to WDR. This confirms the previous statements: the wind-blocking effect is least pronounced for the small, low-rise cubic building while it is most pronounced for the large, wide high-rise building slab.

Next, a comparison is made between the maximum η-values in Table 4 together with those that would be found in free-field conditions, i.e. in a homogeneous wind-flow pattern without building models and hence without disturbances of the wind flow. By Lacy [22], a free-field WDR coefficient ($\kappa_{wdr} = 0.222/R_h^{0.12}$) has been computed. When we multiply this coefficient with the free-field wind speed U_h at building height h, we obtain the free-field catch-ratio value that (theoretically) exists at this height for this wind speed [1]: (Eq. 7).

$$\eta_{free} = \frac{0.222}{R_h^{0.12}} \cdot U_h = \frac{0.222}{R_h^{0.12}} \cdot U_{10} \cdot \left(\frac{h}{10}\right)^{\alpha_P} \tag{7}$$

This operation is now performed for each building. U_h is determined using the power-law expression with α_P = 0.15 and U_{10} = 10 m/s. Table 5 shows the calculation of η_{free} for R_h = 1 mm/h. Fig. 12 illustrates, for each building, the free-field catch ratio η_{free} at height h and the maximum catch ratio η at the building top corner as a function of R_h. Note that the actual η_{CFD}-values are significantly smaller than the free-field values, for all buildings and for almost all R_h, due to the wind-blocking effect. Only for the low-rise cubic building and for heavy rainfall intensities, both values appear to be approximately the same. Table 6 provides numerical values of the ratio (η/η_{free}). For all rainfall intensities, the ratio (η/η_{free}) is smallest for the high-rise slab, higher for the tower building and the medium-rise slab and highest for the low-rise cubic building. These observations are in direct correspondence with the extent of the wind-blocking effect, which is most pronounced for the high-rise slab, somewhat less for the tower and the medium-rise slab and least for the cubic building. Note that the comparison in Figure 12 and in Table 4 and 6 is only conducted for U_{10} = 10 m/s. For other reference wind-speed values, the ratios (η/η_{free}) for each building remain exactly the same, because both η and η_{free} vary linearly with U_{10} and these functions have zero intercept at U_{10} = 0 m/s (see Fig. 8g-h, 9g-h, 10g-h, 11g-h for η and Eq. (7) for η_{free}). As a result, the conclusion of the comparison holds for all reference wind-speed values.

The wind-blocking effect is responsible for the – at first sight – strange observation that the WDR exposure of a low-rise, cubic building (h = 10 m) can be larger than the WDR exposure of a high-rise building slab (h = 60 m) or even a high tower building (h = 80 m). These observations appear to be in contrast to the general notion that the WDR exposure at the top of a building increases with the building height. This notion stems from the fact that the (free-field) wind speed increases with height and that higher wind-speed values yield higher WDR amounts. However, from the calculations in this paper, it is clear that a wider and higher building represents a larger obstruction to the wind-flow pattern (wind blocking) which in turn can cause a lower WDR exposure, even at the top edge of the facade. On the other hand, it must be noted that the simulations were conducted for buildings without surrounding obstructions. In real built environments, buildings seldom stand alone. If we consider a typical European city with many low-rise and medium-rise buildings and with only a few high-rise buildings, the low-rise buildings will generally be sheltered from wind and rain by the other buildings, while the few high-rise buildings will not be sheltered. Therefore, the general notion that high-rise buildings are most exposed to WDR is in reality not necessarily wrong.

The wind-blocking effect also explains some other features of the wetting pattern of the different building configurations: (1) Fig. 8d-f: For the low-rise cubic building: small wind-blocking effect and therefore large η-values over the entire facade. (2) Fig. 9d-f: For the medium-rise wide slab: the small η-values at the lower half of the facade. (3) Fig. 10d-f: For the high-rise slab that presents the largest obstruction to the wind flow: the fact that the lower half of the facade receives little or no rain and that the wetting gradients are only pronounced at the upper part of the facade. (4) Fig. 11d: For the tower building: the small η-values at the lower part of the facade and the fact that the wetting gradients are only pronounced at the upper part of the facade.

The calculation results (wetting patterns) for the high-rise building slab and the tower building and the knowledge about the influence of the wind-blocking effect also serve to answer a frequently asked question amongst researchers and facade designers:

> *"When WDR hits a (non-porous) curtain wall of a high-rise building, when it subsequently runs down the wall and accumulates on its way down, why are large streams of rainwater run-off not observed at the bottom part of the facade (at street level)?"*

Several answers have been suggested in the past, ranging from "evaporation" to "splashing of rainwater running down the wall off the wall by small facade details". Based on the present calculations, we believe that the right answer to this question is the type of wetting pattern: it is highly non-uniform whereby the lower part of the facade receives relatively little WDR. Significant WDR exposure is only present near the top edge of the facade, and the rainwater that runs down from this area is mostly retained as adhesion water by the lower parts of the facade.

7. Discussion

The simulations were conducted with a power-law wind-speed profile with exponent $\alpha_P = 0.15$, corresponding to the roughness of a grass-covered plain. For higher power-law exponents representing rougher terrain and for a certain reference wind speed U_{10}, the increase of wind speed with height above 10 m will be more pronounced and the upstream wind-speed value U_h at building height h (for $h > 10$ m) will significantly increase with the building height (Fig. 13). This will not change the conclusion that the maximum WDR exposure of the facades (at the top corners) is significantly below the free-field WDR exposure. It will also not change the conclusion that the lower part of a high-rise building facade receives relatively little WDR. However, it might lead to the fact that the WDR amount falling at the facade top corners of the higher buildings will become larger than that at the top corner of the lower buildings, even for the lower horizontal rainfall intensities.

An important remark has to be made concerning the free-field exposure as obtained by Lacy's WDR coefficient (Eq. 7). The derivation of this coefficient is based on the assumption of a uniform wind-velocity field ($U(x,y,z)$ = constant), i.e. no increase of wind speed with height (e.g., $\alpha = 0$ for building height $h = 10$ m in Fig. 13). Because in reality the wind speed increases with height and the higher wind-speed values above building height will provide more momentum to the raindrops, Lacy's coefficient and hence Eq. (7) will underestimate the real free-field exposure. This means that the observations made in section 6 will be even more pronounced in reality.

In Figs. 8-11, contour plots for η were only provided for $R_h = 1$, 10 and 30 mm/h. Contour plots for higher R_h-values were not provided because they are quite similar, as indicated for example in Fig. 12 for the top corner position. The reason for this was mentioned in previous research [10]: the catch ratio shows only a low dependency of R_h for R_h larger than about 30 mm/h, irrespective of the location on the building. This is due to two reasons: (1) For rainfall intensities above 30 mm/h, the shape of the raindrop-size distribution does not change very much anymore (Fig. 14). The main observation is the shift of the bulk of raindrop diameters from the interval [2 mm, 3 mm] to higher intervals for higher intensities; (2) The fact that for raindrops with diameters between 2 mm and 6 mm all have approximately the same specific catch ratio, due to their specific shape and drag coefficients [10]. Note that raindrops with diameter larger than 6 mm do not reach the earth's surface, because they are hydrodynamically unstable and break up during their fall [23]. Also note that in this study, already between $R_h = 10$ and 30 mm/h, the differences were quite small.

It is important to note that, although a quite extensive validation of the WDR model has been performed for the low-rise VLIET building, part of which was reported in section 4, no model validation has been performed for the four building configurations that have been addressed in this paper. This is due to the fact that accurate experimental WDR data for different building configurations, including the corresponding measurements of wind speed, wind direction and horizontal rainfall intensity, are very scarce [13]. The strategy that has been followed in this paper corresponds to the general strategy of validation assessment: performing validation studies for those cases for which experimental data are available and then, based on this information, extrapolating the use of the model to similar cases for which no experimental data are available. It is important to note that this strategy also implies that validation studies should be performed whenever possible to increase the reliability and

to increasingly support the extrapolation of the CFD model. Present and future numerical studies of WDR on buildings would greatly benefit from accurate experimental WDR databases, with wind, rain and WDR data on (at least) a 10-minute basis. Obtaining such data for different building configurations and using them to further validate CFD simulations is an important task for the future.

8. Conclusions

CFD simulations were conducted to examine the influence of the wind-blocking effect by a building on its WDR exposure. The term "wind-blocking effect" refers to the disturbance of the wind-flow pattern by the presence of the building and the associated decrease of the upstream streamwise wind-velocity component near the building (wind-speed slow-down). Numerical simulations were made of the WDR distribution on the windward facade of four different building configurations. The conclusion of the study is that the wind-blocking effect is one of the main factors that govern the WDR amount and the WDR distribution pattern on the facades of isolated buildings. It is responsible for the following observations:

1. The maximum WDR exposure of the facades (at the top corners) is significantly below the free-field WDR exposure calculated with Eq. (7) for almost all horizontal rainfall intensities studied. This means that the WDR intensity falling onto the top corners of the facade of an isolated building is lower than the WDR intensity passing through an imaginary vertical plane at the same height, without the building present.
2. The wind-blocking effect will increase when both the height and the width of the building are increased. The influence of this effect on the WDR exposure of the building increases as the horizontal rainfall intensity decreases. Although no systematic investigation of the extent of the wind-blocking effect as a function of building height/width was made, the following conclusions can be drawn:
    a) The larger the wind-blocking effect by the building, the lower the WDR exposure at the building top compared to the free-field WDR exposure. This is true for all horizontal rainfall intensities, from very light (R_h = 0.1 mm/h) to extremely heavy (R_h = 100 mm/h) (see Table 6).
    b) For a given building configuration, the ratio of building-top WDR exposure to free-field WDR exposure decreases significantly as the rainfall intensity decreases (see Table 6). E.g. for the high-rise building slab, it decreases from 65% (for R_h = 100 mm/h) to only 16% (!) (for R_h = 0.1 mm/h).
    c) The larger the wind-blocking effect by the building, the less WDR it will receive at its lower part. This effect becomes more pronounced as the horizontal rainfall intensity decreases. It explains why large streams of rainwater run-off are usually not observed at the bottom part of the facades of high-rise buildings.

Acknowledgements

The first author is a post-doctoral research fellow of the FWO-Flanders (= Research Fund – Flanders; Fonds voor Wetenschappelijk Onderzoek – Vlaanderen). The FWO-Flanders supports and stimulates fundamental research in Flanders (Belgium). Their contribution is gratefully acknowledged. Appreciation is expressed to Wendy Desadeleer for her kind assistance during this research work. The authors also want to thank the anonymous reviewers who provided very valuable suggestions that improved the paper.

Nomenclature

A_f	area of a zone on the building facade (m^2)
A_h	area of a horizontal surface at a certain height in the upstream undisturbed flow (m^2)
b, l, h	building width, length, height (m)
B, L, H	width, length, height of the computational domain (m)
C_d	raindrop drag coefficient (-)
C_{Ks}	roughness constant in the standard wall function modified-for-roughness (-)
$C_{2\varepsilon}$	constant in the realizable k-ε turbulence model (-)
d	raindrop diameter (mm)
E	empirical constant for wall roughness in wall-function method (-)
f(d)	probability-density function of raindrop size in a volume of air (m^{-1})
$f_h(d)$	probability-density function of raindrop size falling through a horizontal plane (m^{-1})
k	turbulent kinetic energy (m^2s^{-2})
K_S	physical roughness height (m)
Re_R	relative Reynolds number (-)
R_h	horizontal rainfall intensity, i.e. through a horizontal plane ($Lm^{-2}h^{-1}$ or mmh^{-1})

R_{wdr}	wind-driven rain intensity ($Lm^{-2}h^{-1}$ or mmh^{-1})
t	time (s)
u^*_{ABL}	friction velocity associated with the inlet profiles of U, k and ε (ms^{-1})
U	streamwise horizontal component of the mean wind-velocity vector (ms^{-1})
U_{10}	reference wind speed at 10 m height in the upstream undisturbed flow (ms^{-1})
U_h	wind speed at building height h in the upstream undisturbed flow (ms^{-1})
V_t	raindrop terminal velocity of fall (ms^{-1})
x, z	streamwise and spanwise co-ordinate (m)
y	height co-ordinate (m)
y_0	aerodynamic roughness length (m)
y_P	distance from the center point of the wall-adjacent cell to the wall (m)
α_P	power-law exponent (-)
ε	turbulence dissipation rate (m^2s^{-3})
η_d	specific catch ratio (-)
η	catch ratio (-)
η_{free}	free-field catch ratio (-)
κ	von Karman constant (≈ 0.42)
κ_{wdr}	free-field wind-driven rain coefficient (sm^{-1})
μ	air dynamic viscosity ($kgm^{-1}s^{-1}$)
ρ	air density (kg/m^3)
ρ_w	water density (kg/m^3)
σ_κ, σ_ε	turbulent Prandtl number for k, ε (-)
φ_{10}	wind direction at 10 m height in the upstream undisturbed flow (degrees from north)
$\vec{V}$	mean wind-velocity vector
$\vec{r}$	position vector of the raindrop in the xyz-space
ABL	Atmospheric Boundary Layer
CFD	Computational Fluid Dynamics
CV	Control Volume
RANS	Reynolds-Averaged Navier-Stokes (equations)
VLIET	Flemish Impulse Programme for Energy Technology
WDR	Wind-Driven Rain

References

[1] B. Blocken, J. Carmeliet, A review on wind-driven rain research in building science, J. Wind Eng. Ind. Aerodyn. 92, 13 (2004) 1079-1130.

[2] C. Souster, A theoretical approach to predicting snow loads and driving rain deposition on buildings, Ph.D. thesis, University of Sheffield, UK, 1979.

[3] E.C.C. Choi, Numerical simulation of wind-driven rain falling onto a 2-D building, Asia Pacific Conf. on Computational Mechanics, Hong Kong, 1991, pp. 1721-1728.

[4] E.C.C. Choi, Simulation of wind-driven rain around a building, J. Wind Eng. Ind. Aerodyn. 46&47 (1993) 721-729.

[5] E.C.C. Choi, Determination of wind-driven rain intensity on building faces, J. Wind Eng. Ind. Aerodyn. 51 (1994) 55-69.

[6] R. Sankaran, D.A. Paterson, Computation of rain falling on a tall rectangular building, J. Wind Eng. Ind. Aerodyn. 72 (1997) 127-136.

[7] H. Hangan, Wind-driven rain studies. A C-FD-E approach, J. Wind Eng. Ind. Aerodyn. 81 (1999) 323-331.

[8] V. Etyemezian, C.I. Davidson, M. Zufall, W. Dai, S. Finger, M. Striegel, Impingement of rain drops on a tall building. Atmos. Environ. 34 (2000) 2399-2412.

[9] F.J.R. Van Mook, Driving rain on building envelopes. Ph.D. thesis. Building Physics Group (FAGO), Eindhoven University of Technology, Eindhoven University Press, Eindhoven, The Netherlands, 2002, 198 p.

[10] B. Blocken, J. Carmeliet, Spatial and temporal distribution of driving rain on a low-rise building, Wind Struct. 5, 5 (2002) 441-462.

[11] E.C.C. Choi, Numerical modeling of gust effect on wind-driven rain, J. Wind Eng. Ind. Aerodyn. 72 (1997) 107-116.

[12] A.C. Best, The size distribution of raindrops, Q. J. Roy. Meteor. Soc. 76 (1950) 16-36.
[13] B. Blocken, J. Carmeliet, High-resolution wind-driven rain measurements on a low-rise building, J. Wind Eng. Ind. Aerodyn. (2005) 93(12): 905-928 (doi:10.1016/j.jweia.2005.09.004)
[14] B. Blocken, J. Carmeliet, On the accuracy of wind-driven rain measurements on buildings, Build. Environ. (2005). In press. (doi:10.1016/j.buildenv.2005.07.022)
[15] J. Wieringa, Updating the Davenport roughness classification, J. Wind Eng. Ind. Aerodyn. 41-44 (1992) 357-368.
[16] T-H. Shih, W.W. Liou, A. Shabbir, J. Zhu, A new k-ε eddy-viscosity model for high Reynolds number turbulent flows – model development and validation, Comp. Fluids 24, 3 (1995) 227-238.
[17] B.E. Launder, D.B. Spalding, The numerical computation of turbulent flows, Comput. Method. Appl. M. 3 (1974) 269-289.
[18] T. Cebeci, P. Bradshaw, Momentum transfer in boundary layers. Hemisphere Publishing Corporation, New York, 1977.
[19] J. Franke, C. Hirsch, A.G. Jensen, H.W. Krüs, M. Schatzmann, P.S. Westbury, S.D. Miles, J.A. Wisse, N.G. Wright. Recommendations on the use of CFD in wind engineering. Proceedings of the International Conference on Urban Wind Engineering and Building Aerodynamics, (Ed. van Beeck JPAJ), COST Action C14, Impact of Wind and Storm on City Life Built Environment, von Karman Institute, Sint-Genesius-Rode, Belgium, 5 - 7 May 2004.
[20] B. Blocken, J. Carmeliet, T. Stathopoulos, A numerical study of the wind speed conditions in passages between buildings and the Venturi-effect, 4th European and African Conference on Wind Engineering (4EACWE), 11-15 July 2005, Prague, Czech Republic. 2005.
[21] R. Gunn, G.D. Kinzer, The terminal velocity of fall for water droplets in stagnant air, J. Meteor. 6 (1949) 243-248.
[22] R.E. Lacy, Driving-rain maps and the onslaught of rain on buildings, RILEM/CIB Symp. Moisture Problems in Buildings, Rain Penetration, Helsinki, Vol. 3, 1965, paper 3-4.
[23] H. Pruppacher, J. Klett, Microphysics of clouds and precipitation, D. Reidel, Boston, 1978.

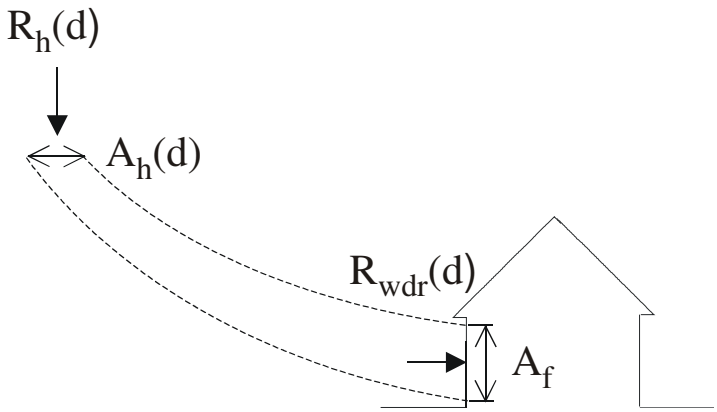

Fig. 1. Stream tube bounded by two raindrop trajectories. The specific catch ratio η_d for zone A_f and for raindrops with diameter d is determined based on conservation of mass for the raindrops in the stream tube.

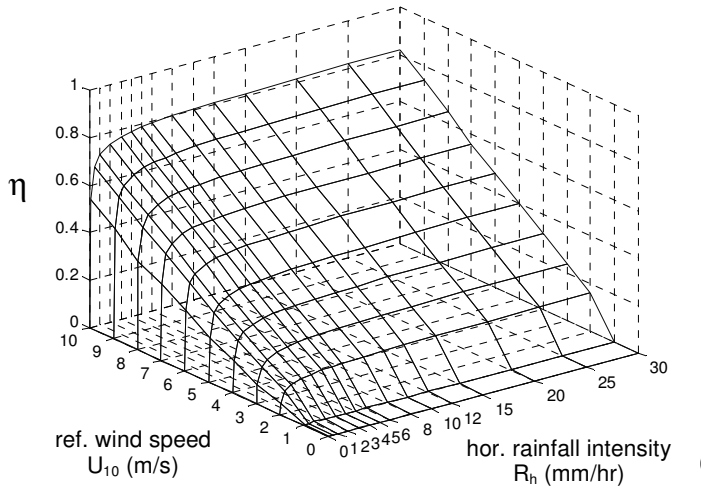

Fig. 2. Typical example of a catch-ratio chart or η-chart that presents the catch ratio η as a function of the reference wind speed U_{10} and the horizontal rainfall intensity R_h, for a given position on the building facade and for a given wind direction.

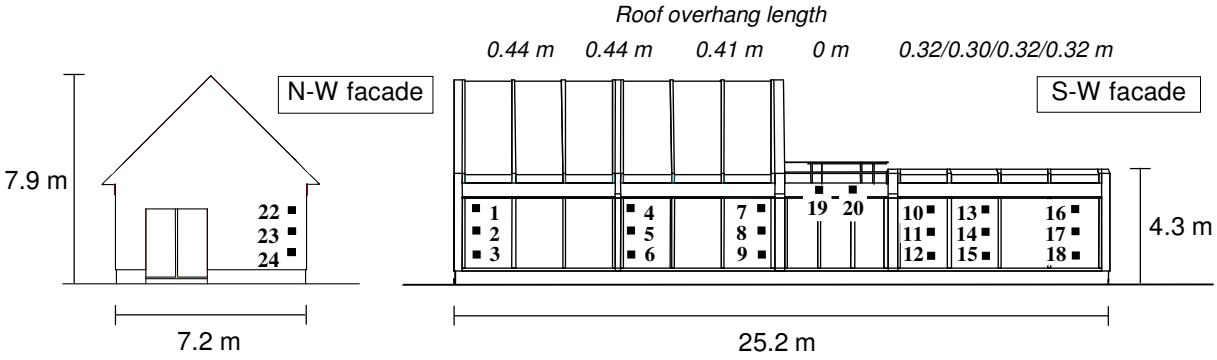

Fig. 3 VLIET test building. North-west and south-west facade. The building dimensions, including roof overhang length, and the positions and numbers of the wind-driven rain gauges (indicated by black squares) are indicated.

Fig. 4. View at the site south-west of the VLIET building. (Photograph taken with the back against the south-west facade).

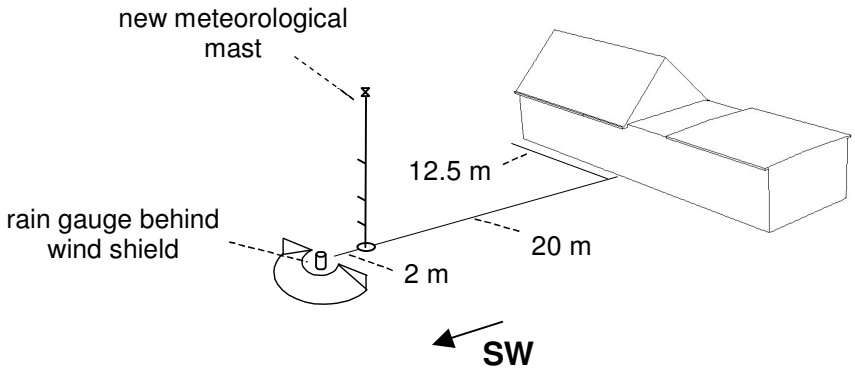

Fig. 5. Meteorological station (mast and horizontal rain gauge) in front of the south-west facade.

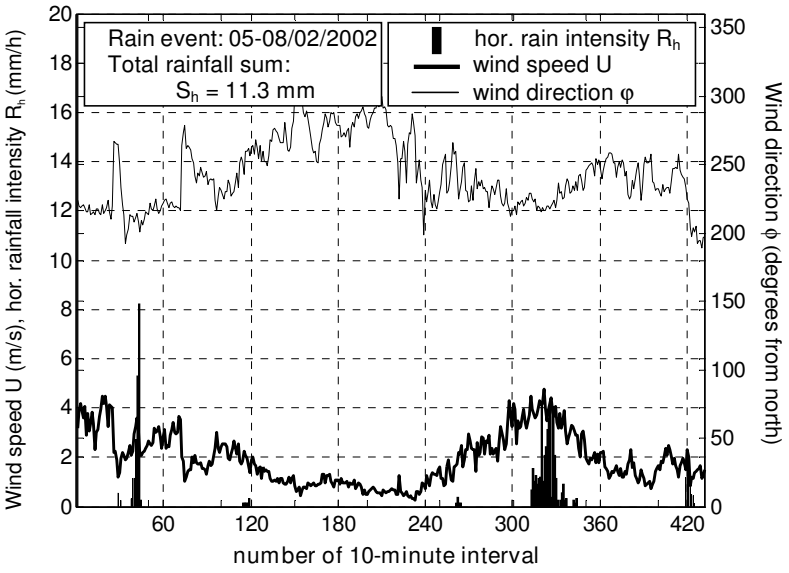

Fig. 6. Meteorological data record of reference wind speed U_{10}, wind direction φ_{10} and horizontal rainfall intensity R_h measured during the rain event (05-08/02/2002). Total horizontal rainfall sum S_h = 11.3 mm.

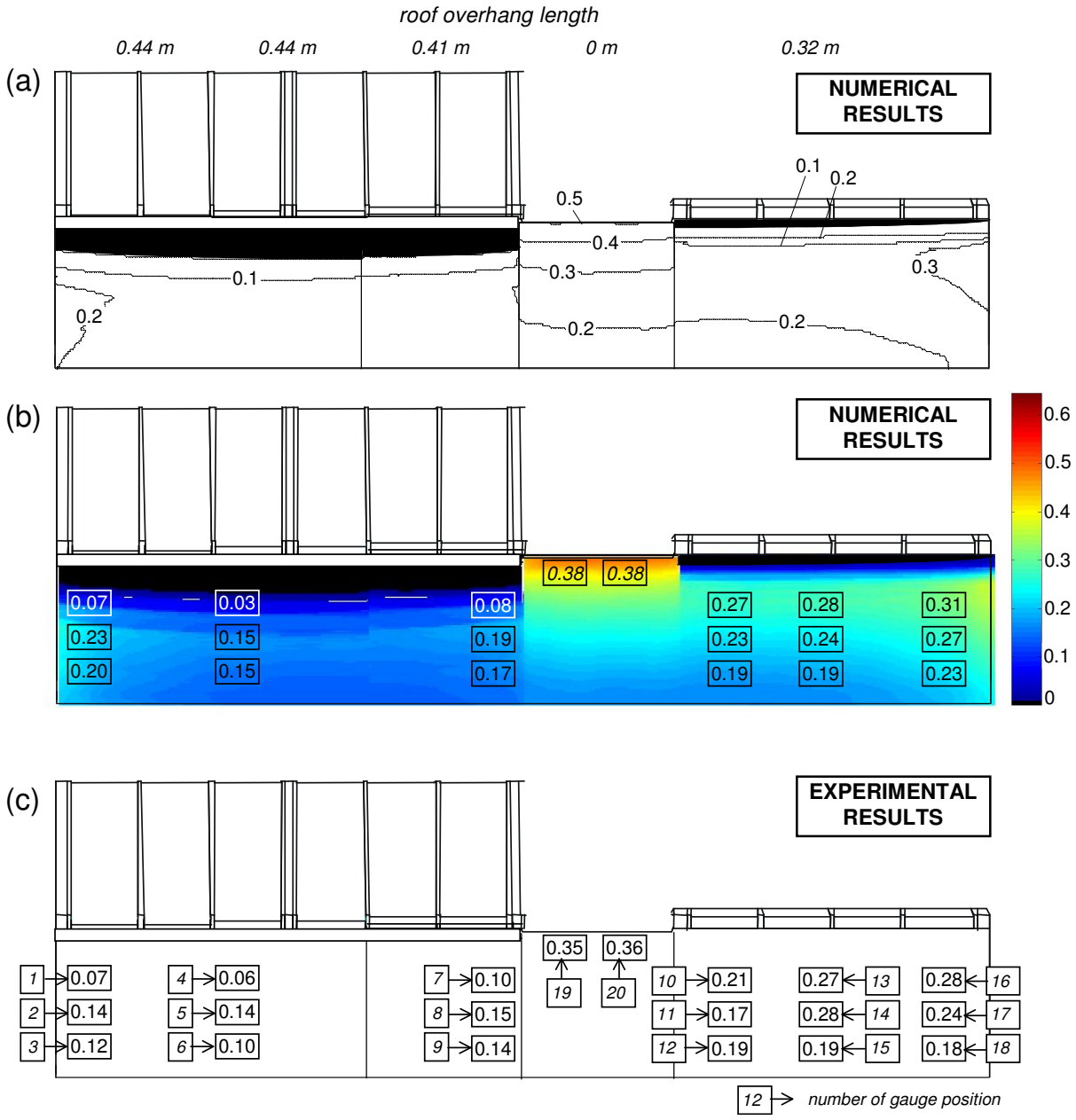

Fig. 7. Spatial distribution of the ratio S_{wdr}/S_h (accumulated wind-driven rain to accumulated horizontal rainfall) for the rain event in Fig. 6. (a-b) Numerical results. Fig. a and b present the same results, but in Fig. b the calculated ratios at the positions of the wind-driven rain gauges are additionally indicated. (c) Experimental results. The measurement error for the ratio S_{wdr}/S_h is 0.05.

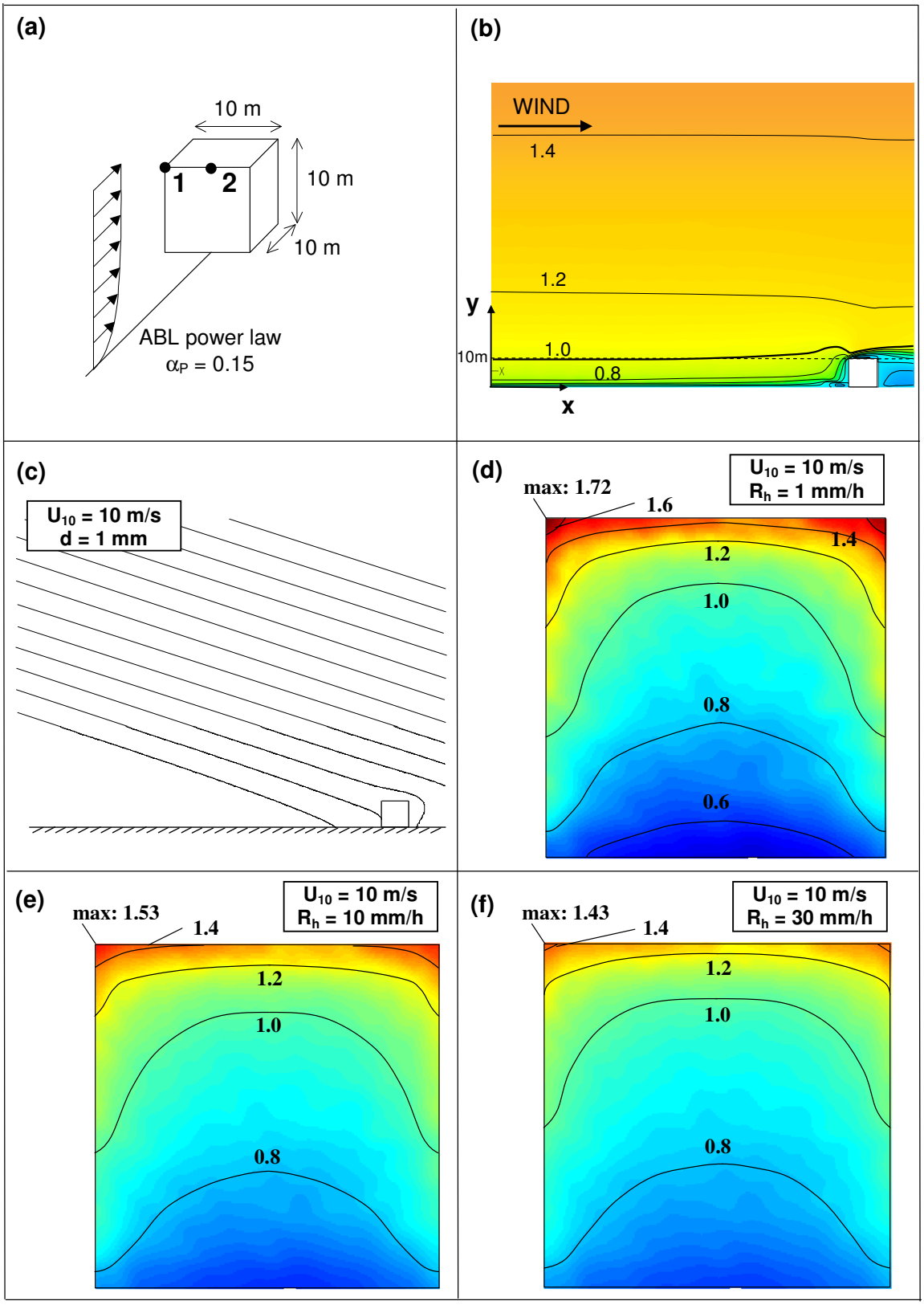

Fig. 8. CFD simulation results of wind-driven rain on the facade of a cubic building model. (a) Building geometry (lxbxh = 10x10x10 m³), approach flow and indication of positions 1 and 2 on the facade. (b) Contours of the streamwise horizontal wind-velocity component (dimensionless: U/U_{10}) in a vertical plane through the center of the building. (c) Raindrop trajectories for U_{10} = 10 m/s and raindrop diameter d = 1 mm in the same vertical plane. (d-f) Catch ratio η on the windward facade for U_{10} = 10 m/s and R_h = 1, 10 and 30 mm/h. (g-h) η-charts for position 1 and 2.

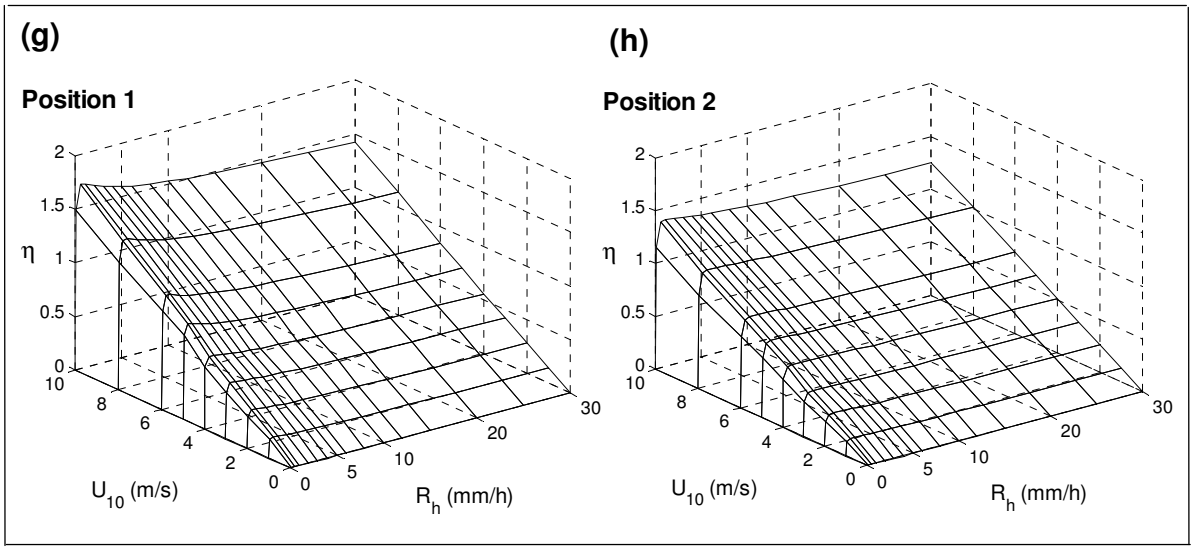

Fig. 8. CFD simulation results of wind-driven rain on the facade of a cubic building model. (a) Building geometry (lxbxh = 10x10x10 m³), approach flow and indication of positions 1 and 2 on the facade. (b) Contours of the streamwise horizontal wind-velocity component (dimensionless: U/U_{10}) in a vertical plane through the center of the building. (c) Raindrop trajectories for U_{10} = 10 m/s and raindrop diameter d = 1 mm in the same vertical plane. (d-f) Catch ratio η on the windward facade for U_{10} = 10 m/s and R_h = 1, 10 and 30 mm/h. (g-h) η-charts for position 1 and 2.

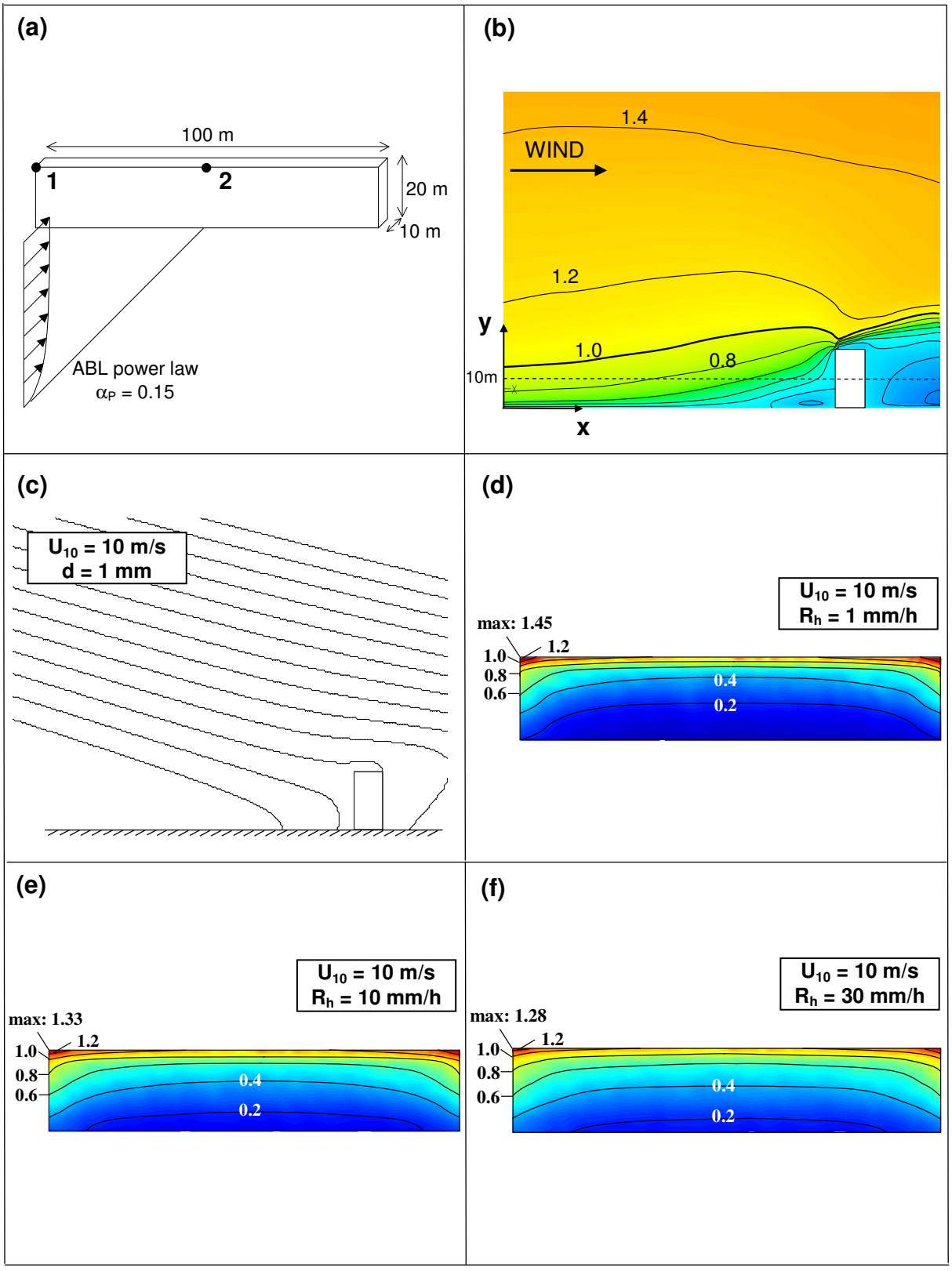

Fig. 9. CFD simulation results of wind-driven rain on the facade of a medium-rise, wide building slab. (a) Building geometry (lxbxh = 100x10x20 m³), approach flow and indication of positions 1 and 2 on the facade. (b) Contours of the streamwise horizontal wind-velocity component (dimensionless: U/U_{10}) in a vertical plane through the center of the building. (c) Raindrop trajectories for U_{10} = 10 m/s and raindrop diameter d = 1 mm in the same vertical plane. (d-f) Catch ratio η on the windward facade for U_{10} = 10 m/s and R_h = 1, 10 and 30 mm/h. (g-h) η-charts for position 1 and 2.

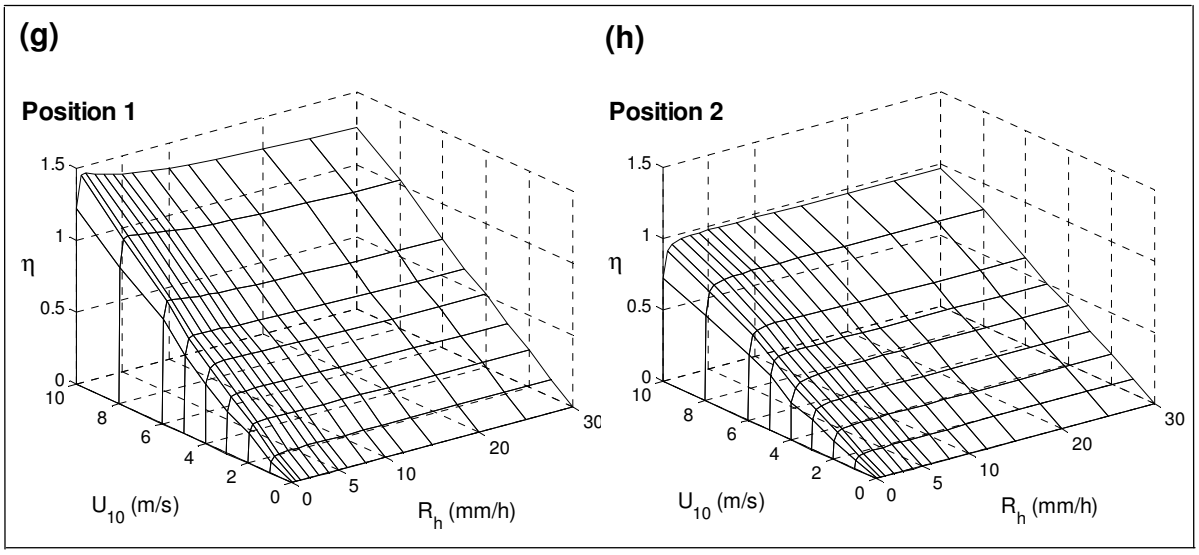

Fig. 9. CFD simulation results of wind-driven rain on the facade of a medium-rise, wide building slab. (a) Building geometry (lxbxh = 100x10x20 m³), approach flow and indication of positions 1 and 2 on the facade. (b) Contours of the streamwise horizontal wind-velocity component (dimensionless: U/U_{10}) in a vertical plane through the center of the building. (c) Raindrop trajectories for U_{10} = 10 m/s and raindrop diameter d = 1 mm in the same vertical plane. (d-f) Catch ratio η on the windward facade for U_{10} = 10 m/s and R_h = 1, 10 and 30 mm/h. (g-h) η-charts for position 1 and 2.

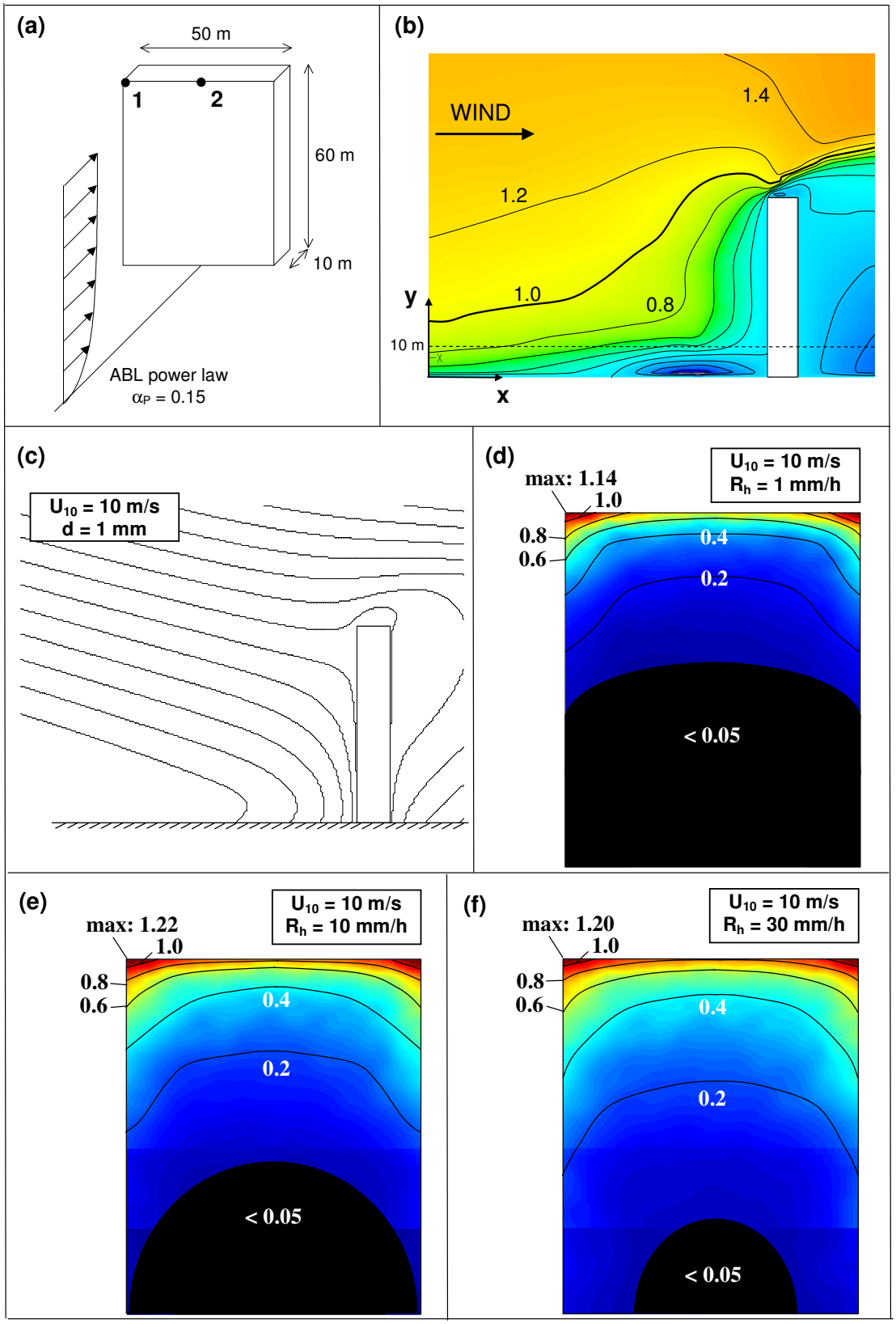

Fig. 10. CFD simulation results of wind-driven rain on the facade of a high-rise building slab. (a) Building geometry (lxbxh = 50x10x60 m³), approach flow and indication of positions 1 and 2 on the facade. (b) Contours of the streamwise horizontal wind-velocity component (dimensionless: U/U_{10}) in a vertical plane through the center of the building. (c) Raindrop trajectories for U_{10} = 10 m/s and raindrop diameter d = 1 mm in the same vertical plane. (d-f) Catch ratio η on the windward facade for U_{10} = 10 m/s and R_h = 1, 10 and 30 mm/h. (g-h) η-charts for position 1 and 2.

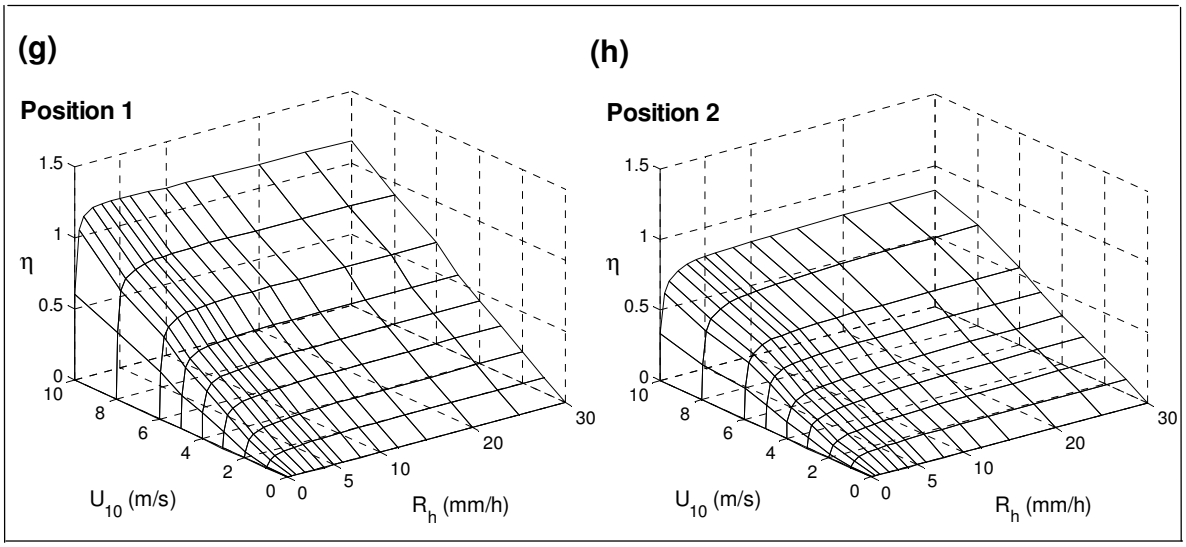

Fig. 10. CFD simulation results of wind-driven rain on the facade of a high-rise building slab. (a) Building geometry (lxbxh = 50x10x60 m³), approach flow and indication of positions 1 and 2 on the facade. (b) Contours of the streamwise horizontal wind-velocity component (dimensionless: U/U_{10}) in a vertical plane through the center of the building. (c) Raindrop trajectories for U_{10} = 10 m/s and raindrop diameter d = 1 mm in the same vertical plane. (d-f) Catch ratio η on the windward facade for U_{10} = 10 m/s and R_h = 1, 10 and 30 mm/h. (g-h) η-charts for position 1 and 2.

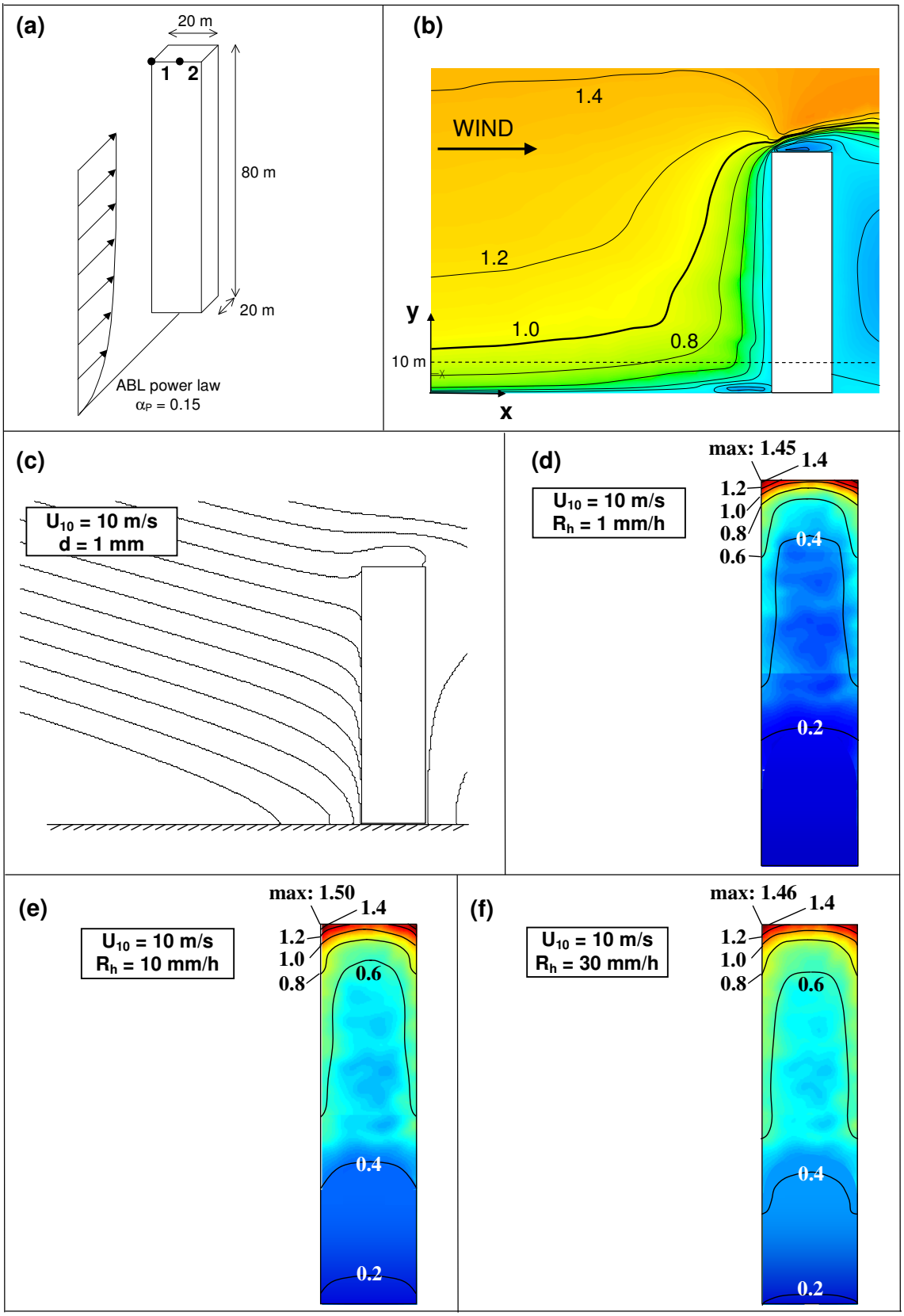

Fig. 11. CFD simulation results of wind-driven rain on the facade of a tower building. (a) Building geometry (lxbxh = 20x20x80 m³), approach flow and indication of positions 1 and 2 on the facade. (b) Contours of the streamwise horizontal wind-velocity component (dimensionless: U/U_{10}) in a vertical plane through the center of the building. (c) Raindrop trajectories for U_{10} = 10 m/s and raindrop diameter d = 1 mm in the same vertical plane. (d-f) Catch ratio η on the windward facade for U_{10} = 10 m/s and R_h = 1, 10 and 30 mm/h. (g-h) η-charts for position 1 and 2.

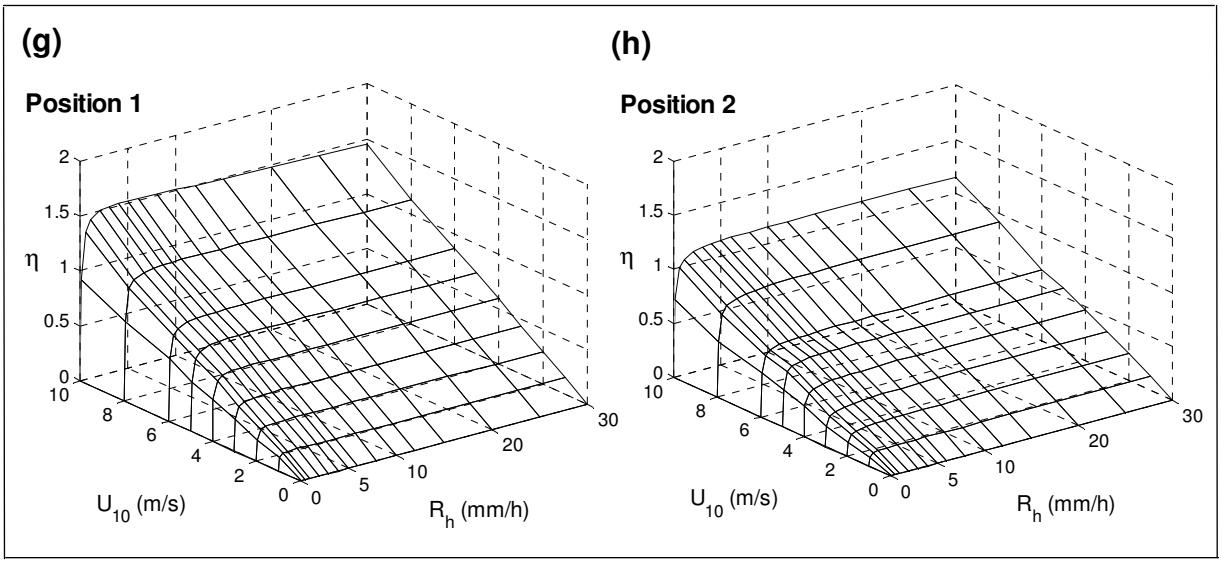

Fig. 11. CFD simulation results of wind-driven rain on the facade of a tower building. (a) Building geometry (lxbxh = 20x20x80 m³), approach flow and indication of positions 1 and 2 on the facade. (b) Contours of the streamwise horizontal wind-velocity component (dimensionless: U/U_{10}) in a vertical plane through the center of the building. (c) Raindrop trajectories for U_{10} = 10 m/s and raindrop diameter d = 1 mm in the same vertical plane. (d-f) Catch ratio η on the windward facade for U_{10} = 10 m/s and R_h = 1, 10 and 30 mm/h. (g-h) η-charts for position 1 and 2.

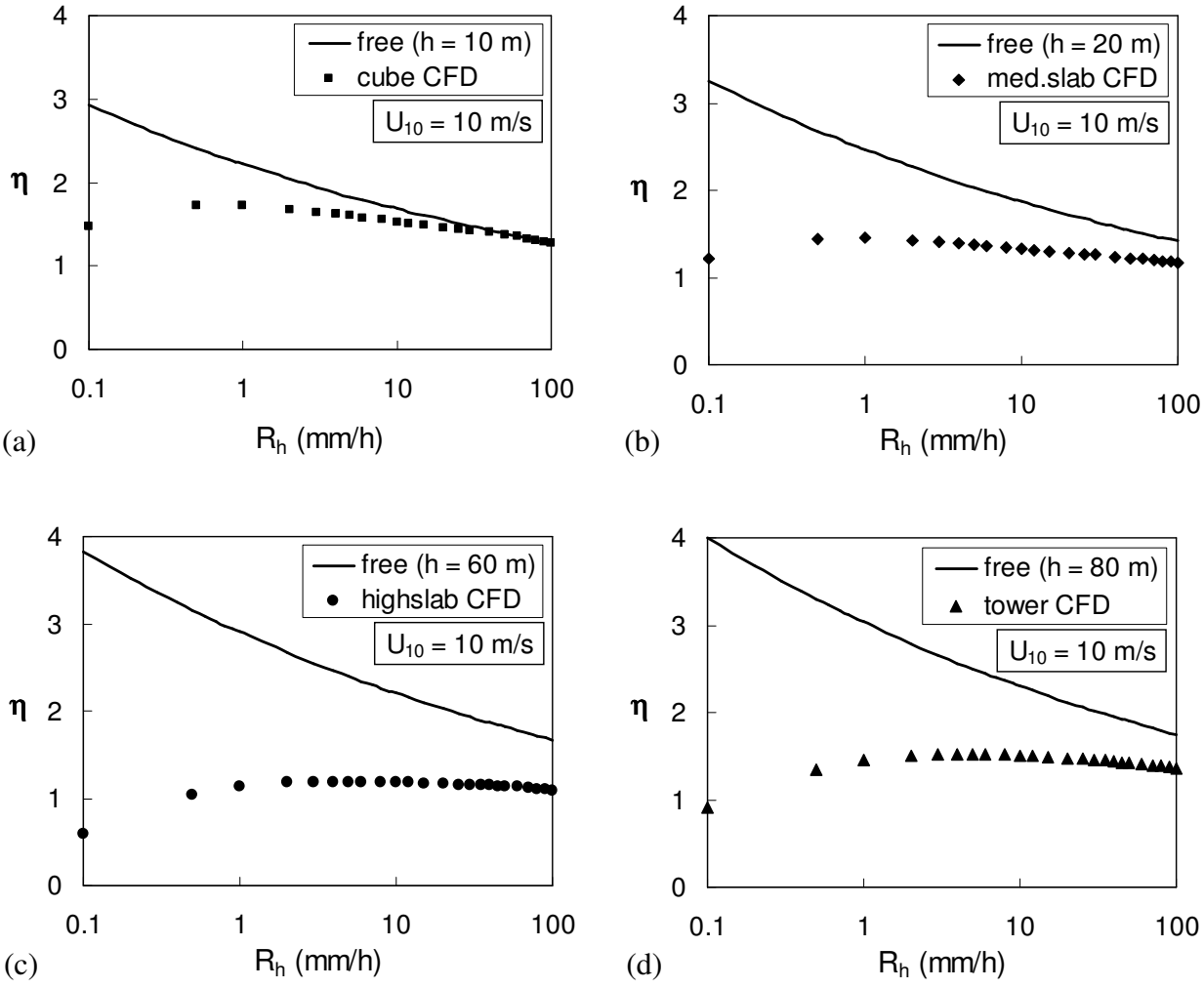

Fig. 12. Comparison of the free-field catch ratio at building height with the maximum catch ratio at the building (top corner position, calculated with CFD) for U_{10} = 10 m/s. (a) low-rise cubic building; (b) medium-rise wide slab; (c) high-rise slab; and (d) tower building.

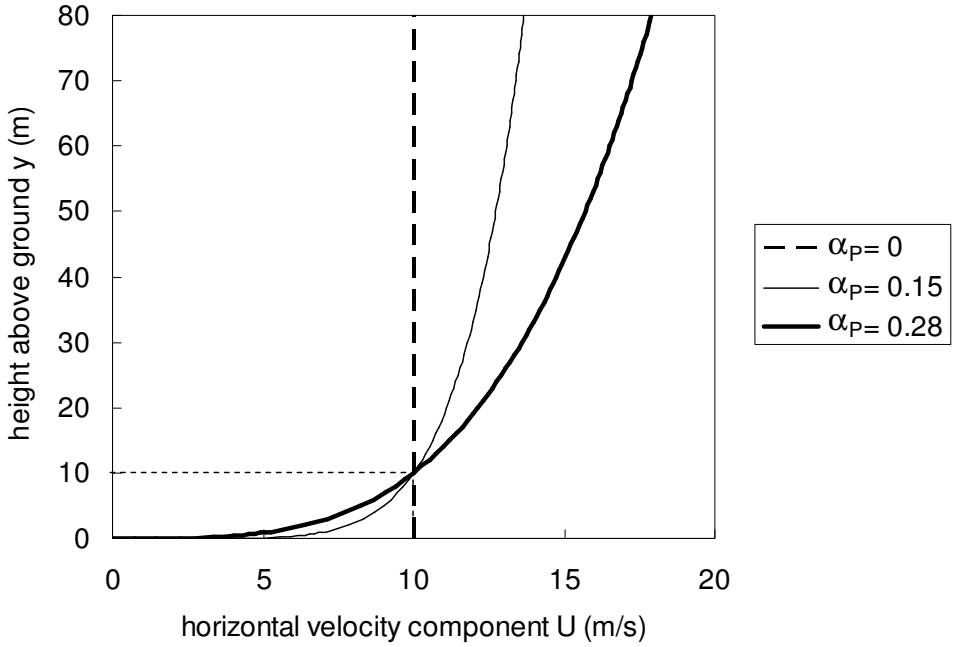

Fig. 13. Power-law wind-speed profiles for U_{10} = 10 m/s, for power-law exponents α_P = 0 (dashed line), α_P = 0.15 (thin solid line) and α_P = 0.28 (thick solid line).

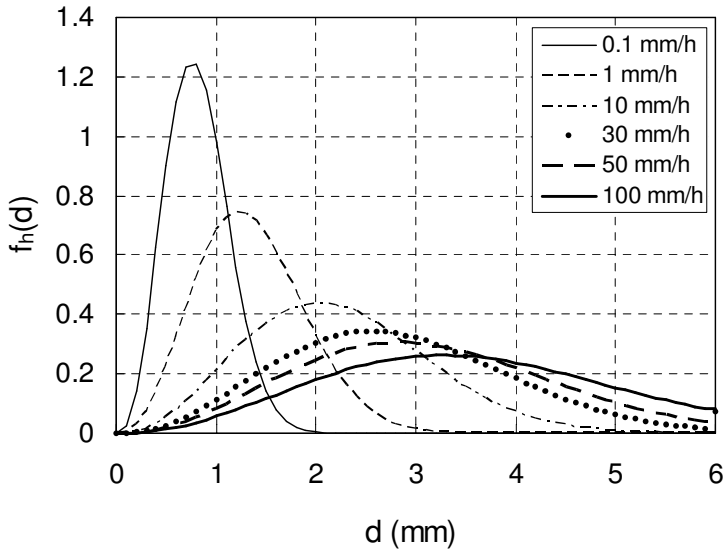

Fig. 14. Raindrop-size distribution $f_h(d)$ through a horizontal plane with the reference rainfall intensity R_h as a parameter – calculated from the raindrop-size distribution in the air according to Best [12].

Table 1: CFD simulation characteristics and settings for wind flow around the VLIET test building

Fluid	
air, incompressible, viscous	
density	1.225 kg/m³
viscosity	1.46E-05 m²/s
static pressure	101320 Pa
Computational domain and mesh	
Geometry	
length	212.2 m
height	50 m
width	89.2 m
Building model	
dimensions:	see Fig. 3
distance from boundaries	
upstream	80 m (*)
downstream	125 m
side	32 m
top	42.1 m
blockage ratio	3.4 %
Mesh	
type: unstructured	
CV type: tetrahedral	
number of CVs	1017518
CV size on build.	0.04 to 0.3 m
min. CV size	0.04 m
max. CV size	6 m
$y_P \approx$	0.01 to 0.25 m
Models	
Turbulence model	
type	realizable k-ε [16]
constants	
$C_{2\varepsilon}$	1.9
σ_κ	1
σ_ε	1.2
Wall functions	
type	standard (modified) [17,18]
constants	
κ	0.42
E	9.81
Boundary conditions	
Inlet	
wind speed	
type	power-law (α_P = 0.176)
U_{10}	10 m/s
u^*_{ABL} (fitted)	0.69 m/s
κ	0.42
y_0 (fitted)	0.03 m
k	$1.5(u^*_{ABL}{}^2)$
ε	$(u^*_{ABL}{}^3)/(\kappa(y+y_0))$
Outlet	
type	pressure outlet
static press.	101320 Pa
Ground surface	
type	wall
method	standard wall funct.
K_S	= y_0 = 0.03 m
C_{Ks}	0.5
Top	
type	symmetry
Operating conditions	
static pressure	101320 Pa
Solver	
segregated, steady, implicit, double precision	
pressure interpolation: standard	
momentum: 2nd order upwind	
pressure-velocity coupling: SIMPLE	
k: 2nd order upwind	
ε: 2nd order upwind	

(*) A relatively large upstream length is needed for the location of the upstream injection positions of the raindrops in the computational domain.

Table 2. Characteristics and settings for the calculation of the raindrop trajectories and the catch ratio, including the integration procedure for Eq. (2) and the integration procedure for Eq. (5) and (6).

Water density ρ_w	1000 kg/m³
Raindrop sizes d	33 discrete diameters; 0.3-1.0 mm in steps of 0.1 mm, 1.0-6.0 mm in steps of 0.2 mm
Raindrop-size distribution f(d)	empirical formula from Best (1950) [12]
Drag coefficient C_d	experimental data from Gunn and Kinzer (1949) [21]
Raindrop terminal velocity V_t	experimental data from Gunn and Kinzer (1949) [21]
Integration procedure Eq. (2)	piecewise analytical with a maximum length-step $\Delta\ell$ = 0.05 m
Integration procedure Eq. (5-6)	discrete, over the 33 raindrop diameters mentioned above, midpoint rule

Table 3. Dimensions of the four rectangular building models

Building model	Length (m)	Width (m)	Height (m)
Low-rise cubic building	10	10	10
Medium-rise slab	100	10	20
High-rise slab	50	10	60
Tower building	20	20	80

Table 4. Comparison of the catch ratio η at the top corner of each building for different horizontal rainfall intensities (U_{10} = 10 m/s, power-law exponent α_p = 0.15).

Building	R_h = 0.1 mm/h	R_h = 1 mm/h	R_h = 10 mm/h	R_h = 30 mm/h	R_h = 100 mm/h
Low-rise cubic building	1.48	1.72	1.53	1.43	1.27
Medium-rise slab	1.22	1.45	1.33	1.28	1.17
High-rise slab	0.6	1.14	1.22	1.20	1.09
Tower building	0.92	1.45	1.50	1.46	1.36

Table 5. Calculation of the free-field catch-ratio values η_{free} for wind speed U_h at building height h (R_h = 1 mm/h, U_{10} = 10 m/s, α_p = 0.15).

Building	h (m)	U_h (m/s)	free-field catch ratio η_{free} (-)
Low-rise cubic building	10	10.0	2.22
Medium-rise slab	20	11.1	2.46
High-rise slab	60	13.1	2.90
Tower building	80	13.7	3.03

Table 6. Comparison of the ratio η/η_{free} for different horizontal rainfall intensities (U_{10} = 10 m/s, α_p = 0.15).

Building	R_h = 0.1 mm/h	R_h = 1 mm/h	R_h = 10 mm/h	R_h = 30 mm/h	R_h = 100 mm/h
Low-rise cubic building	0.51	0.77	0.91	0.97	0.99
Medium-rise slab	0.38	0.59	0.71	0.78	0.83
High-rise slab	0.16	0.39	0.55	0.62	0.65
Tower building	0.23	0.48	0.65	0.72	0.78